Role of the large-scale structures in spanwise rotating plane Couette flow with multiple states

Zhenhua Xia,[1,*] Yipeng Shi,[2] Minping Wan,[3] Chao Sun,[4] Qingdong Cai,[2] and Shiyi Chen[3,2,1,†]
[1]Department of Engineering Mechanics, Zhejiang University, Hangzhou 310027, China
[2]State Key Laboratory for Turbulence and Complex Systems, Center for Applied Physics and Technology, College of Engineering, Peking University, Beijing 100871, China
[3]Department of Mechanics and Aerospace Engineering, Southern University of Science and Technology, Shenzhen 518055, China
[4]Department of Energy and Power Engineering, Tsinghua University, Beijing 100084, China

(Received 1 August 2019; published 22 October 2019)

In the past, dual states were reported in turbulent plane Couette flow with spanwise rotation at $\mathrm{Re}_w = 1300$ and $\mathrm{Ro} = 0.2$ based on direct numerical simulations at a computational box $10\pi h \times 2h \times 4\pi h$, where the flow would evolve to a state with three or two pairs of roll cells if the simulation started with the initial flow field u_i^{3p} or u_i^{2p}. In the present work, the influence of an initial flow field on the dual states is investigated. Nine new simulations with an initial flow field constructed by $u_i = \alpha u_i^{2p} + (1-\alpha)u_i^{3p}$ ($\alpha = 0.1, 0.2, \ldots, 0.9$) are carried out, and it turns out that the flow will evolve to a state with three pairs of roll cells if $\alpha \leqslant 0.6$, while the flow will have only two pairs of roll cells when $\alpha \geqslant 0.7$, which documents the robustness of two states. The turbulent statistics is also revisited, and it is found that the turbulent kinetic energy and related dissipation are larger in the state with more roll cells. The terms in the transport equations of the Reynolds stresses are generally of the same shape at two different states, but the state with more roll cells has a larger value. The energy transfer between the secondary and the residual fields shows that the secondary flows are more energetic at the state with more roll cells while the residual field is more energetic in the other state. Furthermore, a local inverse energy cascade is observed in the near wall region at the latter state with fewer roll cells where the energy is transferred from the residual field to the secondary flow field. Our results support the conjecture that the large-scale secondary flows play a very important role in the dual states of spanwise rotating plane Couette flows.

DOI: 10.1103/PhysRevFluids.4.104606

I. INTRODUCTION

Wall-bounded turbulence subjected to system rotation is of great importance in many astrophysical, geophysical, and engineering applications. It is generally accepted that both the mean flow and the turbulent flow structures will be affected by the system rotation due to the presence of the Coriolis force. Due to the simplicity in geometry, spanwise rotating turbulent channel flows (RTCF) [1–4] and spanwise rotating plane Couette flows (RPCF) [5–9], serving as two canonical cases, have been investigated a lot to study the effect of system rotation on turbulence in the past. In RTCF, the system rotation destabilizes the turbulence in part of the channel while it stabilizes the turbulence in the other part, since the mean vorticity changes its sign across the channel. In contrast, there is

*xiazh@zju.edu.cn
†chensy@sustech.edu.cn

usually no sign change across the channel in RPCF, and the flow is either stabilizing or destabilizing across the whole channel, depending on the direction of the rotation. In the present work, we focus our attention on the latter anticyclonic case in which the system rotation has an opposite sign to the mean flow vorticity.

In the past decades, a lot of work has been carried out to study the flow behaviors in RPCF by numerical simulations [5,6,9–14] or experiments [7,8,15–19]. Tillmark and Alfredsson [15] first conducted experiments of RPCF in both laminar and turbulent regimes, and they reported that the stabilizing rotation with $\mathrm{Ro} < 0$ ($\mathrm{Ro} = 2\Omega_z h/U_w$ is the rotation number, with U_w denoting half of the velocity difference between two walls, Ω_z denoting the constant angular velocity in the spanwise direction, and h denoting the half-channel width) can relaminarize a turbulent flow. They reported a linear relation between the transitional Re_w ($\mathrm{Re}_w = U_w h/\nu$, with ν denoting the kinematic viscosity) and Ro in the (Re_w, Ro) plane, with $\mathrm{Ro} < 0$ and regularly spaced streamwise roll cells at $\mathrm{Re}_w \approx 700$ and $\mathrm{Ro} \approx 0.1$. This work was continued by Alfredsson and Tillmark [16] and Hiwatashi *et al.* [17], and summarized and extended by Tsukahara *et al.* [7]. In their paper, Tsukahara *et al.* [7] performed a systematic experimental investigation on RPCF based on more than 400 previous and current experimental results, covering the range of $0 < \mathrm{Re}_w < 1050$ and $-27 < \Omega < 30$ (here $\Omega = \mathrm{Re}_w\mathrm{Ro}$ is another rotation number used), and they reported a diagram with 17 different flow regimes. Recently, Kawata and Alfredsson [19] studied the momentum transport phenomenon and its dependency on Re_w and Ro. They established a zero absolute vorticity region in the central parts of the channel for high enough rotation rates, and they found that the mean velocity profile exhibited an "S" shape in the center of the channel for certain parameter ranges.

Direct numerical simulations (DNSs) on RPCF were started at almost the same time as the experiments. Bech and Andersson [5] performed DNS on RPCF at $\mathrm{Ro} = \pm 0.01$ and $\mathrm{Re}_w = 1300$ to study the effect of weak system rotation on RPCF, and they found that both senses of rotation damped the turbulence at the low rotation rates considered. They also reported that compared to the nonrotating case, the destabilized flow was more energetic but less three-dimensional due to the kinetic energy extraction of the two-dimensional roll cells from the mean flow. Later, Bech and Andersson [6] investigated the RPCF with strong rotation at $\mathrm{Ro} = 0.1$, 0.2, and 0.5, and they found that the two-dimensional roll cell pattern became more regular and energetic when Ro increased from 0.01 to 0.1 and 0.2, while the flow field was substantially less affected by the roll cells if Ro further increased to 0.5. Barri and Andersson [11] further studied the RPCF at a sufficiently stronger rotation rate $\mathrm{Ro} = 0.7$, and their results indicated that the roll-cell instability was completely suppressed although the turbulence still persisted. Recently, Salewski and Eckhardt [13] performed DNSs on a set of progressively higher Reynolds numbers $\mathrm{Re}_w = 650$, 1300, 2600, and 5200 with varying rotation numbers on a small computational box $4\pi h \times 2h \times 2\pi h$. Their results showed that the momentum flux, which was measured by the wall shear stress, was a nonmonotonic function of Ro at a fixed Re_w in the range $-0.04 \leqslant \mathrm{Ro} \leqslant 0.6$. At lower to moderate Reynolds numbers, a single maximum was observed, while two peaks were discerned at higher Reynolds numbers. Gai *et al.* [9] also carried out a set of DNSs on $\mathrm{Re}_w = 1300$ with Ro varying between 0 and 0.9. They studied the turbulent statistics and flow structures and identified several typical flow regions, and they found a negative mean velocity gradient in the center of the channel at $\mathrm{Ro} = 0.02$, as reported by Salewski and Eckhardt [13] and Kawata and Alfredsson [19]. Huang *et al.* [20] further investigated the flow at $\mathrm{Ro} = 0.02$ with different mesh resolutions and domain sizes, and their results showed that the negative mean velocity gradient would finally disappear if the simulation time was long enough and the streamwise box size $L_x \geqslant 8\pi h$.

Although comprehensive experimental and numerical results have been published in the past 30 years, no multiple turbulent states have been reported in RPCF until very recently; our companion work [14] had documented that multiple states existed in RPCF at $\mathrm{Re}_w = 1300$ and $\mathrm{Ro} = 0.2$ based on DNSs. In fact, multiple states have been reported in several wall-bounded turbulent flows, including transitional boundary layers, Taylor-Couette flows (TCF), and pipe flows [21–26], as well as fully turbulent flows in von Kármán flow [27–29], Rayleigh-Bénard convection [30–35], spherical-Couette flow [36], random Kolmogorov flow [37], forcing rotating turbulence [38], double

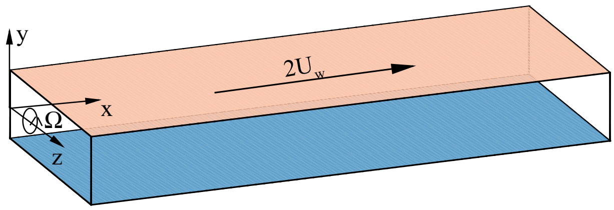

FIG. 1. Sketch of plane Couette flow with spanwise rotation (RPCF).

diffusive convection turbulence [39], as well as TCF at the ultimate turbulence regime [40–44]. In the paper [14], two DNSs at the same control parameter were carried out with the same code on the same computational domain with the same grid resolution. The only differences were the initial flow fields. The very long simulation results showed that the flow statistics, including the mean streamwise velocity and the Reynolds stresses, showed different profiles. At the same time, the flow structures were different, where one state corresponds to two pairs of roll cells while the other shows three pairs in the computation box $L_z = 4\pi h$. This finding was in conflict with the common knowledge on stationary turbulence, where the flow is assumed to be ergodic, and turbulent statistics are unique at fixed control parameters, as stated in [45]: "Even though instantaneous properties in a turbulent flow are extremely sensitive to initial conditions, statistical averages of the instantaneous properties are not." However, the robustness of the multiple states in RPCF and the role of the secondary flows in multiple states remain open questions, and they are the main scope of the present work.

The remainder of the paper is organized as follows. A short review of the numerical methods and the related balance equations are provided in Sec. II. The influences of the initial flow fields will be presented in Sec. III. The turbulent statistics will be discussed again in Sec. IV, including the balances of Reynolds stress transport equations in Sec. IV A and the energy transfer between the secondary and residual fields in Sec. IV B. A summary is given in Sec. V.

II. FLOW CASE DESCRIPTIONS AND EQUATIONS

In the present work, RPCF with incompressible flow is considered. As sketched in Fig. 1, the top wall moves in the streamwise (x) direction with a speed of $2U_w$, while the bottom wall, which is $2h$ below the top one, is fixed. The system rotates in the spanwise (z) direction with a constant angular velocity Ω_z. u, v, and w (or u_1, u_2, and u_3) denote the instantaneous velocities in the streamwise, wall-normal (y), and spanwise directions, respectively. The governing equations are as follows:

$$\frac{\partial u_i}{\partial t} + u_k \frac{\partial u_i}{\partial x_k} = -\frac{1}{\rho}\frac{\partial p}{\partial x_i} + \frac{1}{\mathrm{Re}_w}\frac{\partial^2 u_i}{\partial x_k^2} + \mathrm{Ro}\epsilon_{ik3}u_k, \tag{1}$$

$$\frac{\partial u_k}{\partial x_k} = 0. \tag{2}$$

Hereinafter, the Einstein summation convention is used, p is the effective pressure with the centrifugal effect absorbed, and Reynolds number Re_w and rotation number Ro are

$$\mathrm{Re}_w = \frac{U_w h}{\nu}, \quad \mathrm{Ro} = \frac{2\Omega_z h}{U_w}. \tag{3}$$

As in our previous work [9,14], the above equations (1) and (2) were discretized by using an accurate Fourier-Chebyshev pseudospectral method on a computation domain $10\pi h \times 2h \times 4\pi h$. Periodic boundary conditions are applied in the wall-parallel directions, while the no-slip boundary conditions are adopted at the two walls. The control parameters $\mathrm{Re}_w = 1300$ and $\mathrm{Ro} = 0.2$ are fixed in the present work. In a companion work, Huang *et al.* [46] have shown that the multiple states can exist over a very wide Ro range.

When studying the flow field, the instantaneous velocity and pressure fields can be decomposed into a mean and fluctuating part as

$$u_i(x,y,z,t) = \langle u_i\rangle(y) + u_i'(x,y,z,t),\;\; p(x,y,z,t) = \langle p\rangle(y) + p'(x,y,z,t).$$

Here, $\langle\phi\rangle(y)$ and $\phi'(x,y,z,t)$ denote the temporally and spatially averaged value (TS mean) and the corresponding fluctuation of a quantity $\phi(x,y,z,t)$, respectively. Following this, the equations for the Reynolds stresses $\langle u_i'u_j'\rangle$ can be obtained as follows [3,11,47,48]:

$$\frac{D\langle u_i'u_j'\rangle}{Dt} = \frac{\partial\langle u_i'u_j'\rangle}{\partial t} + \langle u_k\rangle\frac{\partial\langle u_i'u_j'\rangle}{\partial x_k} = P_{ij} + PR_{ij} + T_{ij} + \Pi_{ij} + D_{ij} - \epsilon_{ij} + \mathrm{Rot}_{ij}. \tag{4}$$

Here, the production term P_{ij}, the pressure-strain term PR_{ij}, the triple diffusion term T_{ij}, the pressure diffusion term Π_{ij}, the viscous diffusion term D_{ij}, the dissipation term ϵ_{ij}, and the rotation term Rot_{ij} are defined as

$$P_{ij} = -\langle u_i'u_k'\rangle\frac{\partial\langle u_j\rangle}{\partial x_k} - \langle u_j'u_k'\rangle\frac{\partial\langle u_i\rangle}{\partial x_k},\quad PR_{ij} = \frac{1}{\rho}\left\langle p'\left(\frac{\partial u_i'}{\partial x_j} + \frac{\partial u_j'}{\partial x_i}\right)\right\rangle,$$
$$T_{ij} = -\frac{\partial}{\partial x_k}\langle u_i'u_j'u_k'\rangle,\quad \Pi_{ij} = -\frac{1}{\rho}\frac{\partial}{\partial x_k}\langle p'(u_i'\delta_{jk} + u_j'\delta_{ik})\rangle,$$
$$D_{ij} = \frac{\partial}{\partial x_k}\left(\frac{1}{\mathrm{Re}_w}\frac{\partial\langle u_i'u_j'\rangle}{\partial x_k}\right),\quad \epsilon_{ij} = \frac{2}{\mathrm{Re}_w}\left\langle\frac{\partial u_i'}{\partial x_k}\frac{\partial u_j'}{\partial x_k}\right\rangle,\quad \mathrm{Rot}_{ij} = \mathrm{Ro}\langle\epsilon_{ik3}u_j'u_k' + \epsilon_{jk3}u_i'u_k'\rangle.$$

It should be noticed that the effect of rotation does not enter explicitly in the governing equation of $\langle w'w'\rangle$.

In RPCF, the experimental and numerical studies have shown that the streamwise roll cell structures exist at a certain rotation number range. To study the dynamics of the secondary flows, a triple decomposition approach [5,9,49,50] is introduced to decompose the instantaneous velocity into three parts as

$$u_i(x,y,z,t) = \langle u_i\rangle(y) + u_i'(x,y,z,t) = \bar{u}_i(y,z) + u_i''(x,y,z,t) = \langle u_i\rangle(y) + u_i^s(y,z) + u_i''(x,y,z,t). \tag{5}$$

Here, $\bar{u}_i(y,z)$ is the mean velocity with respect to t and x, and $u_i^s(y,z) = \bar{u}_i(y,z) - \langle u_i\rangle(y)$ denotes the secondary flow part, which usually occurs as roll cells. That is, the fluctuation field u_i' is decomposed into a secondary flow part u_i^s and a residual part u_i''. The fluctuating pressure field can also be decomposed into a secondary part and a residual part. Based on the definition, it is easy to show that the Reynolds stress $\langle u_i'u_j'\rangle$ can be decomposed into two parts,

$$\langle u_i'u_j'\rangle = \langle u_i^s u_j^s\rangle + \langle u_i''u_j''\rangle. \tag{6}$$

Thus, the turbulent kinetic energy $k = \langle u_i'u_i'\rangle/2$ and the Reynolds shear stress $R_{12} = -\langle u_1'u_2'\rangle$ can be separated into two parts,

$$k = \tfrac{1}{2}\langle u_i'u_i'\rangle = \tfrac{1}{2}\langle u_i^s u_i^s\rangle + \tfrac{1}{2}\langle u_i''u_i''\rangle = k^s + k'',$$
$$R_{12} = \langle u_1'u_2'\rangle = \langle u_1^s u_2^s\rangle + \langle u_1''u_2''\rangle = R_{12}^s + R_{12}'',$$

i.e., the ones from the secondary flow field (k^s and R_{12}^s) and the ones from the residual flow field (k'' and R_{12}'').

The kinetic energy of the secondary flow can further be split into a streamwise part $k_u^s = \langle u^s u^s\rangle/2$ and a cross-flow part $k_{vw}^s = (\langle v^s v^s\rangle + \langle w^s w^s\rangle)/2$, which can be viewed as a consequence of the quad-decomposition of the velocity [5,9,48,51],

$$(u,v,w) = (\langle u\rangle,\langle v\rangle,\langle w\rangle) + (u^s,0,0) + (0,v^s,w^s) + (u'',v'',w'').$$

The transport equations for k_u^s, k_{vw}^s, and k'' can be easily obtained from the definition of the decompositions and the Navier-Stokes equations. They are of the following forms [5,48,51]:

$$\frac{Dk_u^s}{Dt} = \underbrace{-\frac{d}{dy}\left\langle\frac{1}{2}u^s u^s v^s\right\rangle}_{T_u^s} \underbrace{-\frac{d\langle u^s\overline{u''v''}\rangle}{dy}}_{T_{1,u}^s} + \underbrace{\frac{d}{dy}\left(\frac{1}{\mathrm{Re}_w}\frac{dk_u^s}{dy}\right)}_{D_u^s}$$
$$\underbrace{-\langle u^s v^s\rangle\frac{d\langle u\rangle}{dy}}_{P_u^s} \underbrace{-\frac{1}{\mathrm{Re}_w}\left\langle\frac{\partial u^s}{\partial x_k}\frac{\partial u^s}{\partial x_k}\right\rangle}_{\epsilon_u^s} + \underbrace{\left\langle\overline{u''u_k''}\frac{\partial u^s}{\partial x_k}\right\rangle}_{T_{2,u}^s} + \underbrace{\mathrm{Ro}\langle u^s v^s\rangle}_{\mathrm{Rot}^s}, \tag{7}$$

$$\frac{Dk_{vw}^s}{Dt} = \underbrace{-\frac{d}{dy}\left\langle\frac{1}{2}(v^s v^s + w^s w^s)v^s\right\rangle}_{T_{vw}^s} \underbrace{-\frac{d\langle v^s\overline{v''v''} + w^s\overline{v''w''}\rangle}{dy}}_{T_{1,vw}^s} + \underbrace{\frac{d}{dy}\left(\frac{1}{\mathrm{Re}_w}\frac{dk_{vw}^s}{dy}\right)}_{D_{vw}^s} \underbrace{-\frac{d\langle p^s v^s\rangle}{dy}}_{\Pi^s}$$
$$\underbrace{-\frac{1}{\mathrm{Re}_w}\left\langle\frac{\partial v^s}{\partial x_k}\frac{\partial v^s}{\partial x_k} + \frac{\partial w^s}{\partial x_k}\frac{\partial w^s}{\partial x_k}\right\rangle}_{\epsilon_{vw}^s} + \underbrace{\left\langle\overline{v''u_k''}\frac{\partial v^s}{\partial x_k} + \overline{w''u_k''}\frac{\partial w^s}{\partial x_k}\right\rangle}_{T_{2,vw}^s} - \underbrace{\mathrm{Ro}\langle u^s v^s\rangle}_{\mathrm{Rot}^s}, \tag{8}$$

$$\frac{Dk''}{Dt} = \underbrace{-\frac{d}{dy}\left\langle\frac{1}{2}\overline{u_i''u_i''v''}\right\rangle}_{T''} \underbrace{-\frac{d}{dy}\left\langle\frac{1}{2}\overline{u_i''u_i''}v^s\right\rangle}_{T_1''} + \underbrace{\frac{d}{dy}\left(\frac{1}{\mathrm{Re}_w}\frac{dk''}{dy}\right)}_{D''} \underbrace{-\frac{d\langle p''v''\rangle}{dy}}_{\Pi''}$$
$$\underbrace{-\langle u''v''\rangle\frac{d\langle u\rangle}{dy}}_{P''} \underbrace{-\frac{1}{\mathrm{Re}_w}\left\langle\frac{\partial u_i''}{\partial x_k}\frac{\partial u_i''}{\partial x_k}\right\rangle}_{\epsilon''} \underbrace{-\left\langle\overline{u_i''u_k''}\frac{\partial u_i^s}{\partial x_k}\right\rangle}_{T_2''}. \tag{9}$$

The summation of Eqs. (7) and (8) will arrive at the transport equation for k^s. Note that the rotation term Rot^s acts as a sink for the transport equation of k_u^s while it is the main source for k_{vw}^s, and that $T_2'' + T_{2,u}^s + T_{2,vw}^s = 0$, illustrating that these three terms are the energy transfer between the secondary flows and the residual field.

As pointed out in Ref. [14], the secondary flows will be weakened apparently if the traditional triple decomposition (5) is adopted due to the locomotion of roll cells in the spanwise direction. To accurately capture the secondary flows, a roll-cell-fixed averaging procedure was introduced to perform the triple decomposition. That is, the flow field is first shifted in the spanwise direction to make sure that the roll cells are in phase before performing the traditional triple decomposition. Since the flow is periodic in the spanwise direction, the shift of the whole field will not break the basic relations of the traditional triple decomposition, and the above equations are still working for the present analysis.

III. INFLUENCE OF INITIAL FLOW FIELDS

Before investigating further the transport equations for the Reynolds stresses and the energy transfer between the secondary flows and the residual field, we would like first to ascertain the robustness of the dual states in RPCF by changing the initial flow fields. The simulations are carried out at the same computation domain $10\pi h \times 2h \times 4\pi h$ with the same grid resolution $256 \times 97 \times 256$, and we had shown in Ref. [14] that this grid resolution is fine enough to accurately capture the multiple states. The initial flow fields are constructed as

$$u_i = \alpha u_i^{2p} + (1-\alpha)u_i^{3p}, \tag{10}$$

as what was done in Ref. [38]. Here, the initial fields u_i^{2p} and u_i^{3p} are the final snapshots of the simulations in Ref. [14] where the flow has two pairs of roll cells and three pairs of roll cells,

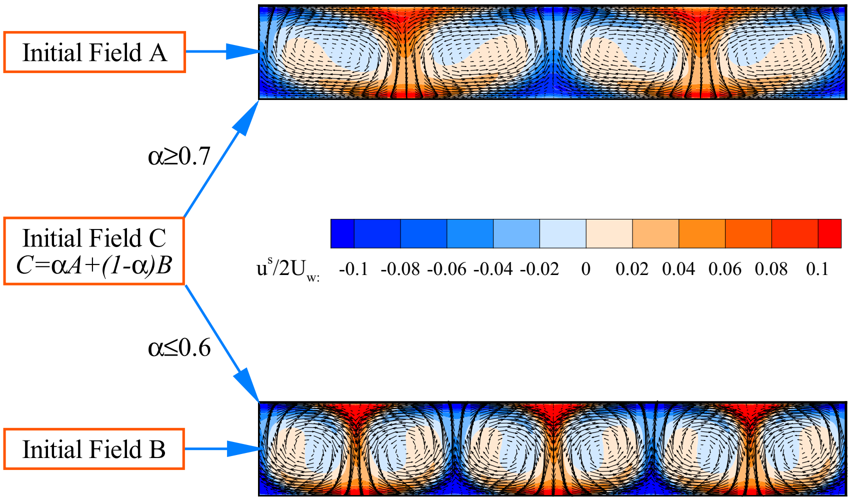

FIG. 2. A sketch of Roll cells with different initial flow fields. Initial field A refers to u_i^{2p}, where the flow will evolve to a state with two pairs of roll cells, while B refers to u_i^{3p}, where the flow will be of three pairs of roll cells.

respectively, and $\alpha \in [0, 1]$ is the weight of the interpolation between u_i^{2p} and u_i^{3p}. It should be noted that the present construction method, i.e., the linear combination of two different solutions, to investigate the influence of initial fields could be useful in general. The newly constructed field fulfills the continuity equation (2) since u_i^{2p} and u_i^{3p} satisfy the continuity equation. The flow fields at future steps are obtained by following the NS equations. Therefore, the present superposition of the different flow fields is reasonable. In the present work, all of the nine simulations with $\alpha = 0.1, 0.2, \ldots, 0.9$ were run for a time duration of $1500h/U_w \approx 47.7L_x/U_w$. The flow statistics were performed by using 1501 flow fields with sampling time interval $\Delta T = 0.5h/U_w$ in the second half of the simulations.

Figure 2 shows the number of roll cells with different initial flow fields. The roll cells are obtained by the same procedure as in Ref. [14]. It turns out that the flow will evolve to a three-pair state if $\alpha \leqslant 0.6$, while it will evolve to a two-pair state when $\alpha \geqslant 0.7$. A boundary that separates the two-pair state and the three-pair state exists in the range $0.6 < \alpha < 0.7$. In the work by Yokoyama and Takaoka [38], they found that the separating boundary of the bistable quasi-two-dimensional and three-dimensional states exists in the range $0.2 < \alpha < 0.3$. They speculated that the separatrix might be a thick and blurred region. Similarly, we are not aiming to find the exact value of the separatrix, but we illustrate the robustness of the multiple states with different initial flow fields.

Figure 3(a) shows the streamwise TS mean velocity $\langle u(y)\rangle$ at different weights $\alpha = 0.1, 0.3, 0.6, 0.7$, and 0.9, and Fig. 3(b) shows the velocity difference from $\alpha = 0.9$ at $\alpha = 0.2, 0.4, 0.5$, and 0.8. It is evident from the figure that there are two sets of mean velocity profiles. One is with a larger mean shear rate at the centerline where $\alpha \leqslant 0.6$, and the other is flatter around the center region with $\alpha \geqslant 0.7$. The differences depicted in Fig. 3(b) further illustrate that the two sets of mean velocity profiles are indeed different almost everywhere across the channel, and the biggest difference is around $0.04U_w$ at $y \approx \pm 0.95h$, which cannot be ignored. The two sets of mean velocity profiles match with the previous results shown in Ref. [14], where the state with two pairs of roll cells (which corresponds to $\alpha = 1.0$) has a flatter mean velocity in the center part of the channel, while the one with three pairs (i.e., $\alpha = 0$) has a larger mean shear rate at the centerline.

Figure 4 shows the normalized diagonal components of Reynolds stresses $\langle u'u'\rangle$ (a), $\langle v'v'\rangle$ (b), and $\langle w'w'\rangle$ (c), and the normalized Reynolds shear stress $-\langle u'v'\rangle$ (d) (by $4U_w^2$) from different simulations. Again, the data show two different sets of behaviors. One is with $\alpha \leqslant 0.6$, and the

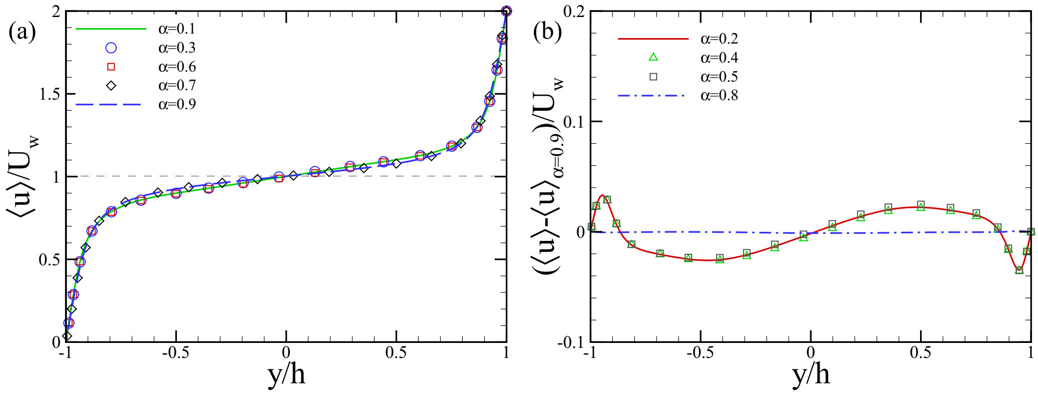

FIG. 3. (a) Mean velocity profiles for $\alpha = 0.1$, 0.3, 0.6. 0.7, and 0.9; (b) mean velocity differences from $\alpha = 0.9$ for $\alpha = 0.2$, 0.4, 0.5, and 0.8.

other is with $\alpha \geqslant 0.7$. For $\langle u'u' \rangle$ and $\langle w'w' \rangle$, the largest differences occur in the near wall region, which are $y/h \approx \pm 0.9$ and $y/h \approx \pm 0.8$, respectively. However, for $\langle v'v' \rangle$, the largest differences are located at the centerline, and for $-\langle u'v' \rangle$, the differences are almost constant at $-0.5 \lesssim y/h \lesssim 0.5$. From the above results, it can be concluded that the two turbulent states are quite robust to its initial conditions.

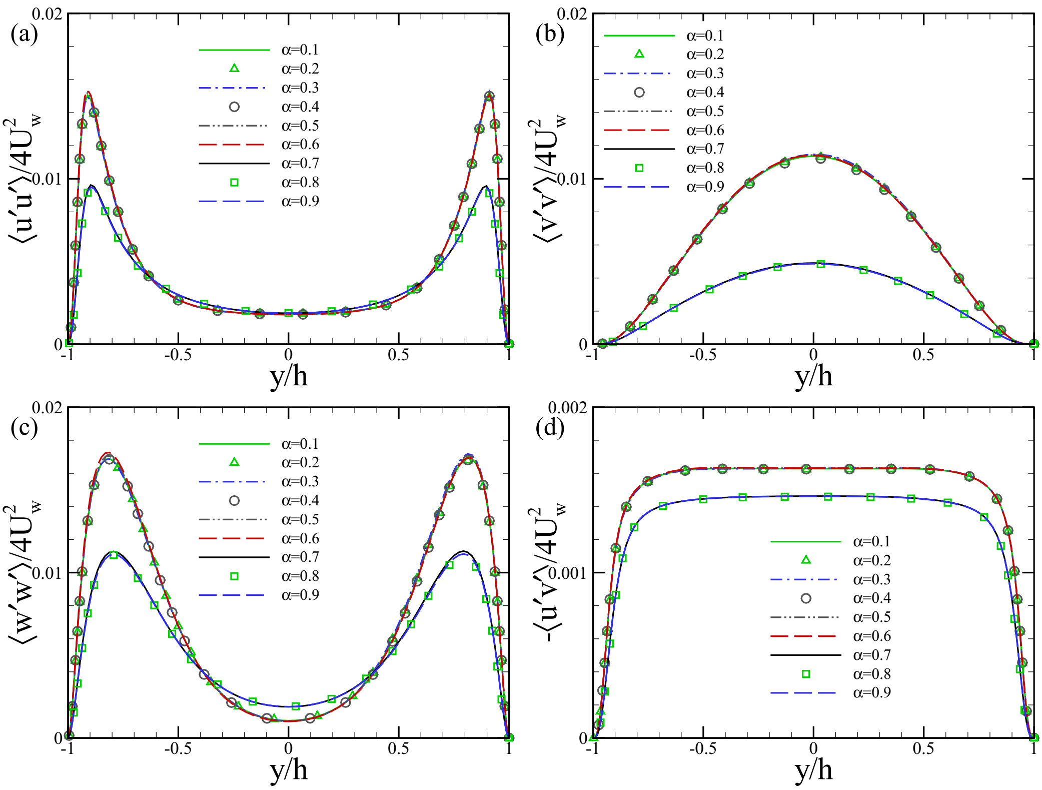

FIG. 4. Reynolds stresses from all simulations: (a) $\langle u'u' \rangle$; (b) $\langle v'v' \rangle$; (c) $\langle w'w' \rangle$; and (d) $-\langle u'v' \rangle$. All quantities are normalized by $4U_w^2$.

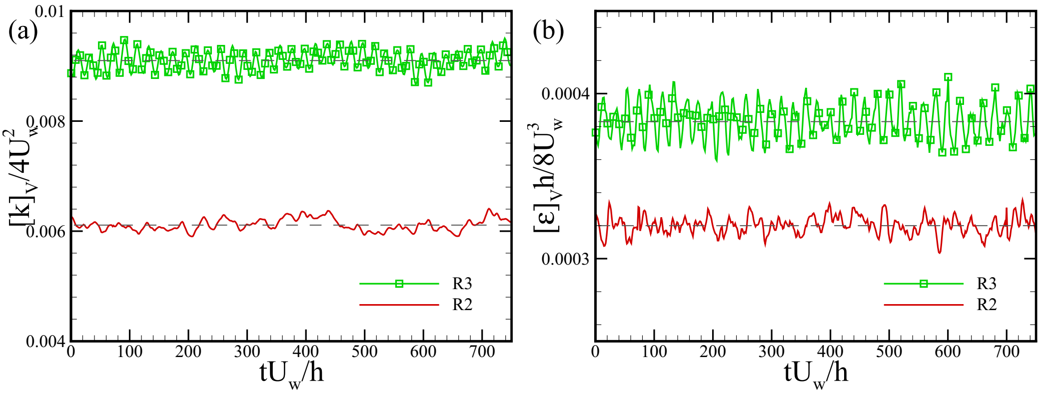

FIG. 5. Time series of (a) volume-averaged turbulent kinetic energy $[k]_V$ (normalized by $4U_w^2$) and (b) volume-averaged dissipation $[\varepsilon]_V$ (normalized by $8U_w^3/h$) from the two-pair state and the three-pair state.

IV. TURBULENT STATISTICS

In this section, the turbulent statistics at different states will be investigated, and our focuses are the balance of Reynolds stresses and the energy transfer between the secondary flows and the residual field. The results with a grid resolution $256 \times 97 \times 256$ will be shown. Before moving forward, we would like first to study the volume-averaged turbulent kinetic energy and dissipation at two different states.

Figure 5 shows the time series of the volume-averaged turbulent kinetic energy $[k]_V$ and dissipation $[\varepsilon]_V$ at the two-pair state (denoted as "$R2$") and the three-pair state (denoted as "$R3$"). Here,

$$[\phi]_V(t) = \frac{1}{2hL_xL_z}\int_{-h}^{h}\int_0^{L_x}\int_0^{L_z}\phi(x,y,z,t)dz\,dx\,dy$$

denotes the volume-averaged value of a quantity $\phi(x,y,z,t)$. It is interesting to observe that both quantities at the $R3$ state are much larger than those at the $R2$ state. For $[\varepsilon]_V$, the mean value at the $R3$ state ($\approx 0.003\,06U_w^3/h$) is about 19.5% larger than that at the $R2$ state ($\approx 0.002\,56U_w^3/h$). For $[k]_V$, the difference is about 49.2% ($0.0364U_w^2$–$0.0244U_w^2$), illustrating that the $R3$ state is more energetic in turbulence than the $R2$ state. In fact, as shown in Figs. 4(a)–4(c) [see also Figs. 4(a)–4(c) in [14]], all three shares of the turbulent kinetic energy are generally larger at the $R3$ state than those at the $R2$ state, except at the center region, where $\langle u'u'\rangle$ and $\langle w'w'\rangle$ are slightly larger at the $R2$ state. In the following subsection, we are going to study the balance of the Reynolds stress transport equation and the transfer of the kinetic energy between the secondary and the residual fields.

A. Balance of the Reynolds stress transport equation

Figures 6–9 show the terms of the transport equation for the four nonzero components in the Reynolds stresses $\langle u'u'\rangle$, $\langle v'v'\rangle$, $\langle w'w'\rangle$, and $\langle u'v'\rangle$, respectively. The results from cases $R3$ and $R2$ are compared with each other. It is seen that there is no apparent dominance region in the balance equations for all four components at two different states, which is in sharp contrast to those in RPCF at Ro $= 0.7$ [11] or those in spanwise rotating channel flow [3]. For $\langle u'u'\rangle$ as shown in Fig. 6, the main differences occur in the near wall region $y/h < -0.8$ for D_{11}, P_{11}, $-\epsilon_{11}$, and T_{11}, and the absolute values from the $R3$ state are much larger than those from the $R2$ state. At the wall, D_{11} and $-\epsilon_{11}$ from case $R3$ are almost twice the values from case $R2$. Very slight differences can be observed for the other part of the channel and for the other two quantities. For the wall-normal component $\langle v'v'\rangle$ as shown in Fig. 7, the quantities T_{22}, Π_{22}, and PR_{22} have larger

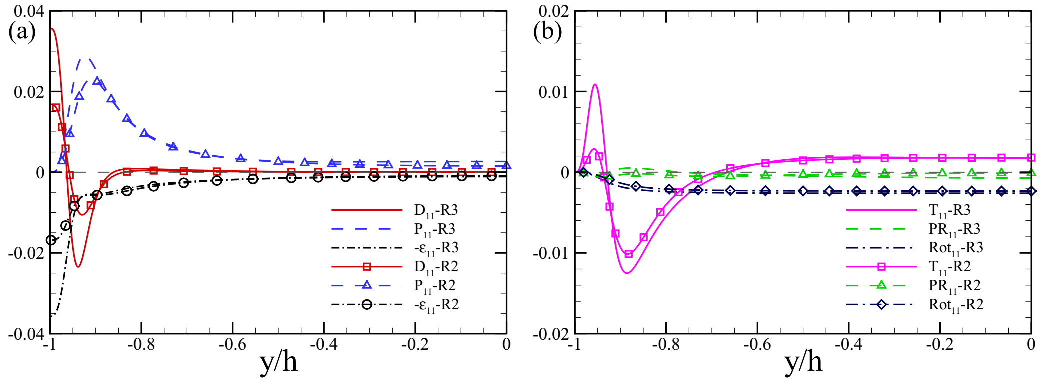

FIG. 6. The terms of the transport equation for $\langle u'u'\rangle$ from two different states: (a) D_{11}, P_{11}, and $-\epsilon_{11}$; (b) T_{11}, PR_{11}, and Rot_{11}. All quantities are normalized by $8U_w^3/h$.

values than the other three terms across the channel. Π_{22} redistributes the energy share $\langle v'v'\rangle$ in the region $-0.8 < y/h < -0.35$ to the near wall and channel center regions, and the share to the near wall region is balanced by PR_{22}. Again, the quantities are generally larger in value for case $R3$, and this is similar for the results of $\langle w'w'\rangle$ and $\langle u'v'\rangle$ at different states, which are depicted in Figs. 8 and 9.

Now, we are considering the time-volume-averaged balance equations for the Reynolds stresses. Denoting

$$[\phi]_y = \frac{1}{2h}\int_{-h}^{h}\phi(y)dy,$$

the time-volume-averaged balance equation for $[\langle u_i'u_j'\rangle]_y$ can be obtained from Eq. (4) as

$$[P_{ij}]_y + [PR_{ij}]_y + [\mathrm{Rot}_{ij}]_y - [\epsilon_{ij}]_y = 0, \tag{11}$$

due to the fact that the time-volume-averaged diffusion terms

$$[T_{ij}]_y = 0, \quad [\Pi_{ij}]_y = 0, \quad [D_{ij}]_y = 0,$$

i.e., they only redistribute the quantities. The other nonzero terms from two different cases are listed in Table I. It is evident that the above equation (11) is valid for all four components at two different

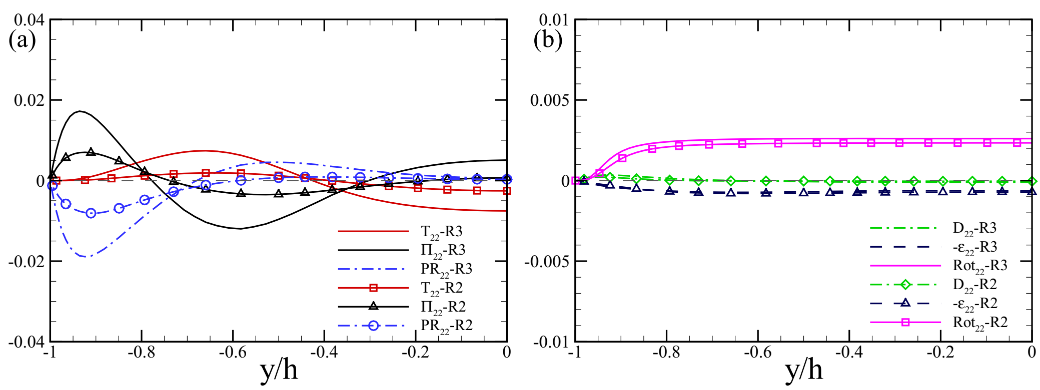

FIG. 7. The terms of the transport equation for $\langle v'v'\rangle$ from two different states: (a) T_{22}, Π_{22}, and PR_{22}; (b) D_{22}, $-\epsilon_{22}$, and Rot_{22}. All quantities are normalized by $8U_w^3/h$.

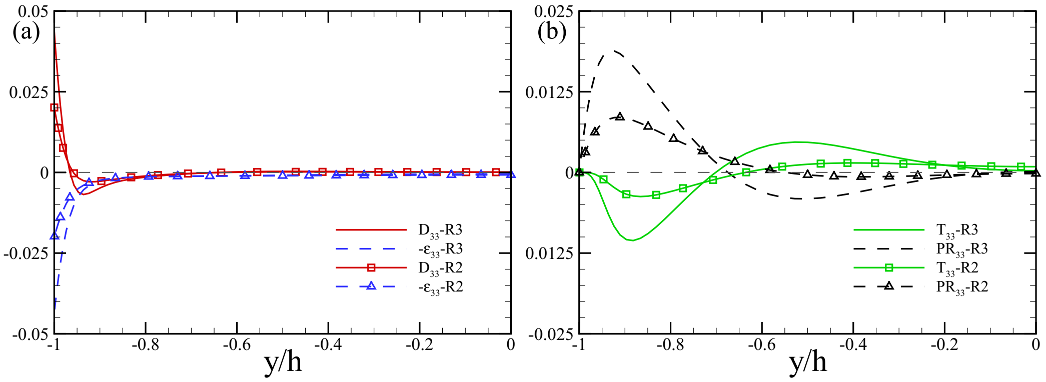

FIG. 8. The terms of the transport equation for $\langle w'w' \rangle$ from two different states: (a) D_{33} and $-\epsilon_{33}$; (b) T_{33} and PR_{33}. All quantities are normalized by $8U_w^3/h$.

cases, and imbalance is negligible. The three diagonal components can be viewed as the share of the kinetic turbulent energy due to the fact that $2k = \langle u'u' \rangle + \langle v'v' \rangle + \langle w'w' \rangle$. Therefore, more balance relations can be obtained:

$$[P_{11}]_y - [\epsilon_{11}]_y - [\epsilon_{22}]_y - [\epsilon_{33}]_y = 0, \quad [PR_{11}]_y + [PR_{22}]_y + [PR_{33}]_y = 0.$$

Thus, we may draw a picture of the balance and transfer of turbulent kinetic energy between the three components. The production term $[P_{11}]_y$ draws energy from the mean field and deposits it into the turbulence fluctuation field. A big share of it (more than 50%) is dissipated by the streamwise component $[\epsilon_{11}]_y$. Other shares are transferred to the wall-normal component through the rotation term $[\mathrm{Rot}_{11}]_y$ (around 40%) and the spanwise component through the pressure-strain term $[PR_{11}]_y$. For the wall-normal component, the energy transferred from the streamwise component is balanced by two parts, a small share (around a quarter), which is dissipated by the viscosity, and a big share, which is transferred to the spanwise component through the pressure-strain term $[PR_{22}]_y$. For the spanwise component, the energy received from the streamwise and wall-normal components is balanced by the viscosity dissipation. This picture of the balance and transfer of turbulent kinetic energy between the three components is the same for cases $R2$ and $R3$. However, $[P_{11}]_y = 7.663$ at the $R3$ state, which is larger than $[P_{11}]_y = 6.403$ at the $R2$ state, illustrating that the energy drawn from the mean field by turbulence at the $R3$ state is larger than that at at $R2$ state, leading to larger

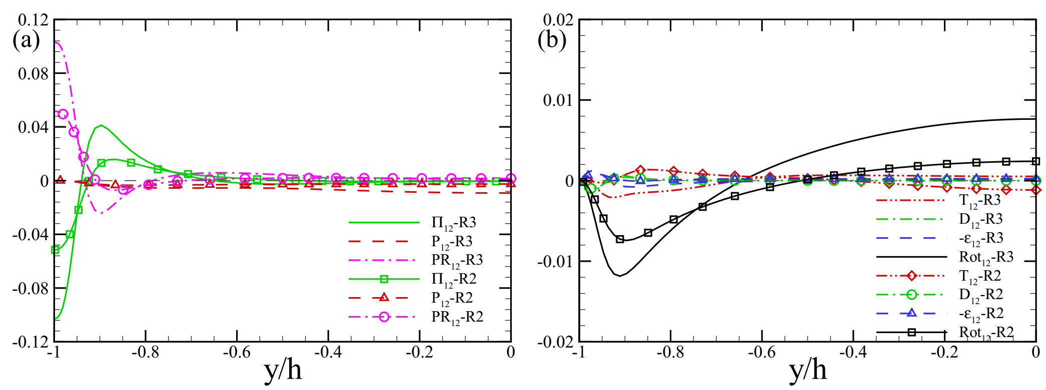

FIG. 9. The terms of the transport equation for $\langle u'v' \rangle$ from two different states: (a) Π_{12}, P_{12}, and PR_{12}; (b) T_{12}, D_{12}, $-\epsilon_{12}$, and Rot_{12}. All quantities are normalized by $8U_w^3/h$.

TABLE I. Wall-normal averaged quantities from the balance equations of Reynolds stresses from two different states. All quantities are normalized by $8U_w^3/h$ and amplified by 10^4.

	$R3$				$R2$			
Quantities	$[P_{ij}]_y$	$-[\epsilon_{ij}]_y$	$[PR_{ij}]_y$	$[\mathrm{Rot}_{ij}]_y$	$[P_{ij}]_y$	$-[\epsilon_{ij}]_y$	$[PR_{ij}]_y$	$[\mathrm{Rot}_{ij}]_y$
$i=1, j=1$	7.663	−4.260	−0.452	−2.949	6.403	−3.465	−0.347	−2.591
$i=2, j=2$		−0.770	−2.177	2.949		−0.848	−1.739	2.591
$i=3, j=3$		−2.634	2.628			−2.092	2.086	
$i=1, j=2$	−7.766	0.017	6.072	1.659	−3.308	0.256	4.038	−0.999

values of energy transfers between the three components, i.e., $[\mathrm{Rot}_{11}]_y$ and $[PR_{22}]_y$, and thus the larger value of $[\langle u'u'\rangle]_y$, $[\langle v'v'\rangle]_y$, and $[\langle w'w'\rangle]_y$ at the $R3$ state, and this is consistent with the larger kinetic energy and dissipation of the turbulence field at the $R3$ state as shown in Fig. 5.

For the time-volume-averaged balance of $[\langle u'v'\rangle]_y$, the differences between the two states are more obvious. As discussed before, the larger production term $[P_{11}]_y$ at the $R3$ state will lead to a larger value of $[\langle v'v'\rangle]_y$, and thus a larger magnitude of $[P_{12}]_y$ since $P_{12} = -\langle v'v'\rangle d\langle u\rangle/dy$ at the $R3$ state. This larger absolute value of $[P_{12}]_y$ will result in larger values of $-[\langle u'v'\rangle]_y$ and $[P_{11}]_y$ at the $R3$ state in return, which forms a closed circle of arguments. Another significant difference between the two states is the role of $[\mathrm{Rot}_{12}]_y$. At the $R3$ state, it is positive, meaning that $[\langle u'u'\rangle]_y < [\langle v'v'\rangle]_y$. On the other hand, $[\mathrm{Rot}_{12}]_y < 0$ at the $R2$ state, and thus the time-volume-averaged streamwise kinetic energy is still dominant over the wall-normal component.

B. Transfer of energy between secondary and residual flows

In the preceding subsection, the balances of the Reynolds stress transport equations were presented, and the results show that the profiles are nearly with the same pattern while the magnitudes at the $R3$ state are generally larger than those at the $R2$ state, resulting in larger quantities

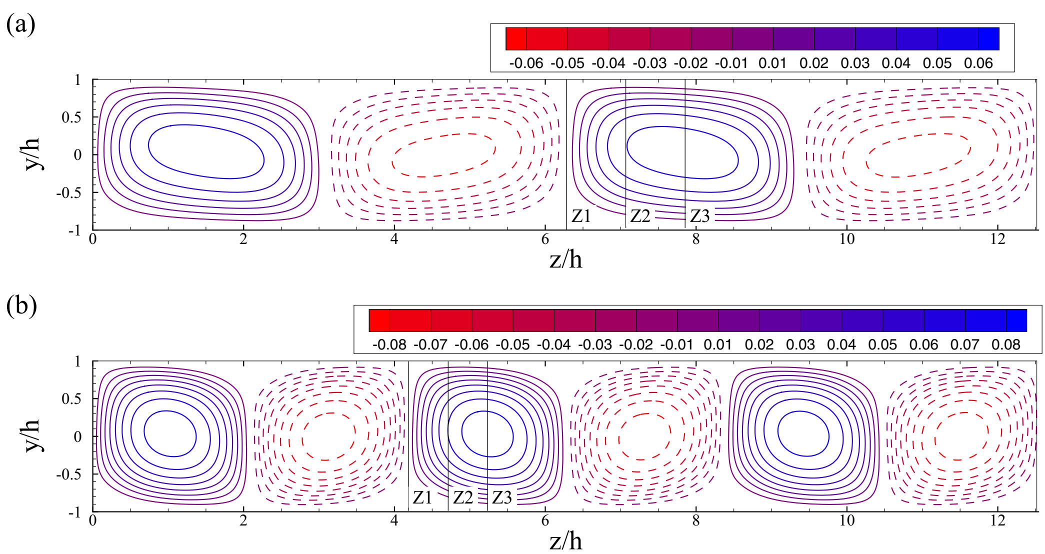

FIG. 10. Contours of the stream function Ψ (normalized by $2U_w h$) corresponding to the cross-flow of the secondary flows (v^s, w^s) from two different states: (a) $R2$ state with peak values $\Psi \approx \pm 0.064$ and (b) $R3$ state with peak values $\Psi \approx \pm 0.086$. The solid lines are the levels with $\Psi > 0$ while the dashed lines show the levels with $\Psi < 0$. The three vertical solid lines show the locations of local profiles shown in Fig. 11.

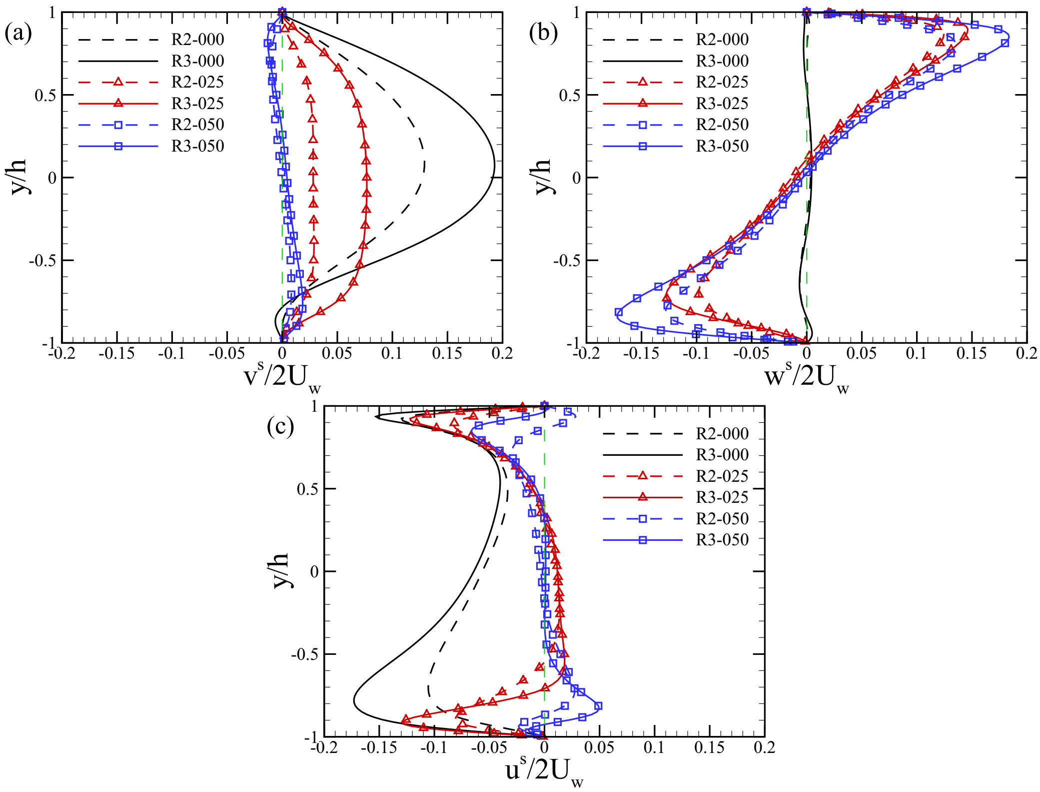

FIG. 11. Profiles of the secondary flow field at three locations $Z1$ (denoted by "000"), $Z2$ (denoted by "025"), and $Z3$ (denoted by "050") indicated in Fig. 10: (a) wall-normal component v^s; (b) the spanwise component w^s, and (c) the streamwise component u^s. All quantities are normalized by $2U_w$.

of the time-volume-averaged terms at the $R3$ state. In this subsection, we will investigate the energy transfer between the secondary and residual flows, aiming at exploring the role of the secondary flows at two different states.

Before moving forward, the characteristics of the roll cell structures are first investigated. Figure 10 shows the contours of the stream function Ψ corresponding to the cross-flow of the secondary flows (v^s, w^s) at two different states. Ψ is obtained to make sure that it is zero on the wall and

$$v^s = \frac{\partial \Psi}{\partial z}, \quad w^s = -\frac{\partial \Psi}{\partial y}.$$

As seen from the contours shown in the figure, where the solid and dashed contours represent $\Psi > 0$ and $\Psi < 0$, respectively, there are two and three pairs of roll cells in the $R2$ and $R3$ states, respectively. The roll cells are not in a perfectly circular shape and they are stretched in certain directions. Furthermore, the density of the streamlines is higher in the zone in which the fluid leaves the near-wall region than in the stagnation regions where the fluid approaches the wall [6], and the density is also higher at the $R3$ state than at the $R2$ state, which means that the roll cells are stronger at the $R3$ state, which is consistent with the larger k^s_{vw} discussed below. To further characterize the differences of the roll cells, the profiles of v^s, w^s, and u^s at three locations, i.e., the centerline between one pair of roll cells, a quarter of one roll cell, and a half of one roll cell, are shown in Fig. 11. Generally, all profiles from two different states at the same location are the same in shape but different in magnitude. For the wall-normal component v^s, it is seen that it is largest at the $Z1$

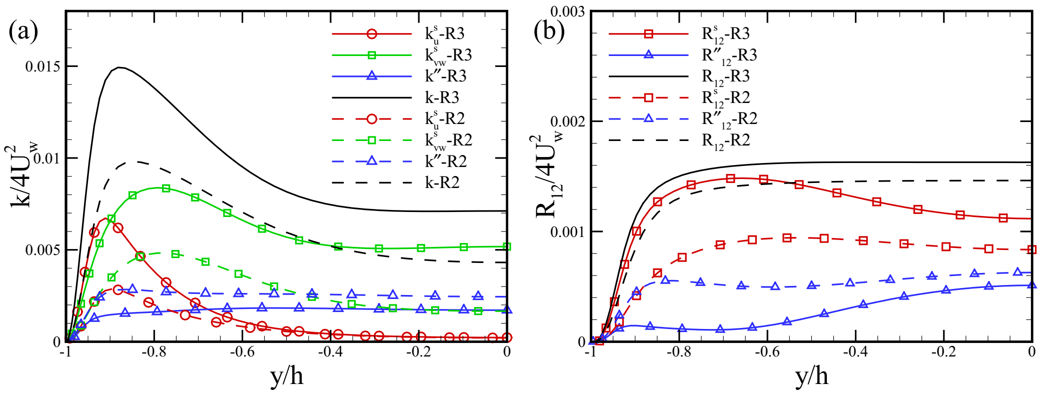

FIG. 12. (a) Profiles of total kinetic energy k and its three shares k_u^s, k_{vw}^s, and k'', and (b) profiles of total Reynolds shear stress R_{12} and its two shares R_{12}^s and R_{12}'' from two different states. All quantities are normalized by $4U_w^2$.

location while it is very close to zero at the $Z3$ location. However, it is opposite for the spanwise component w^s, where it has the largest value at the $Z3$ location. For the streamwise component u^s, there is generally a similar trend to that of v^s. This means that the roll cells can bring down the higher-speed fluid from the top wall and bring up lower-speed fluid from the bottom [14]. An important point to notice from the profiles of v^s and w^s at $Z1$ is that a slightly negative (positive) region can be observed for v^s (w^s) at $-1 < y/h < -0.8$ at the $R3$ state, illustrating that there are other small secondary vortices in that region [9]. However, these small secondary vortices can hardly be observed at the $R2$ state.

Figure 12(a) shows the profiles of the total kinetic energy k and its three shares, i.e., the streamwise part k_u^s, and the cross-flow part k_{vw}^s from the secondary flows and the residual flow field k'', from two different states. It is seen that k_{vw}^s at the $R3$ state is larger (nearly twice) than that at the $R2$ state across the whole channel, while k_u^s is larger at the $R3$ state at $-1 < y/h < -0.5$, resulting in a much larger contribution of the secondary flow $k^s = k_u^s + k_{vw}^s$. In contrast, k'' at the $R3$ state is smaller than that at the $R2$ state. However, the difference in the kinetic energy from the secondary flows between two states dominates over that from the residual field, which leads to a higher total kinetic energy k at the $R3$ state. Similar results can be observed for the Reynolds shear stress as shown in Fig. 12(b), that is, the contribution from the secondary flows is the same as the total one while the contribution from the residual field shows an opposite trend. The wall-normal averaged kinetic energy, Reynolds shear stress, and their shares from the secondary flows and residual flows are listed in Table II. Consistent with the profiles, the shares from the secondary flows, $[k_u^s]_y$, $[k_{vw}^s]_y$, and $[R_{12}^s]_y$, are much larger at the $R3$ state, dominating over those from the residual flows, although they are larger in value at the $R2$ state. The above results illustrate that the secondary flows may play a very important role in these two states.

To further explore the role of the secondary flows, we display in Fig. 13 the production terms of the secondary flows and the residual flows, and the energy transfer term among the streamwise

TABLE II. Wall-normal averaged quantities of the kinetic energy and Reynolds shear stress and the corresponding shares from two different states. All quantities are normalized by $4U_w^2$ and amplified by 10^3.

States	$[k_u^s]_y$	$[k_{vw}^s]_y$	$[k'']_y$	$[k]_y$	$[R_{12}^s]_y$	$[R_{12}'']_y$	$[R_{12}]_y$
$R3$	1.597	5.852	1.658	9.107	1.206	0.269	1.475
$R2$	0.877	2.765	2.475	6.117	0.781	0.514	1.295

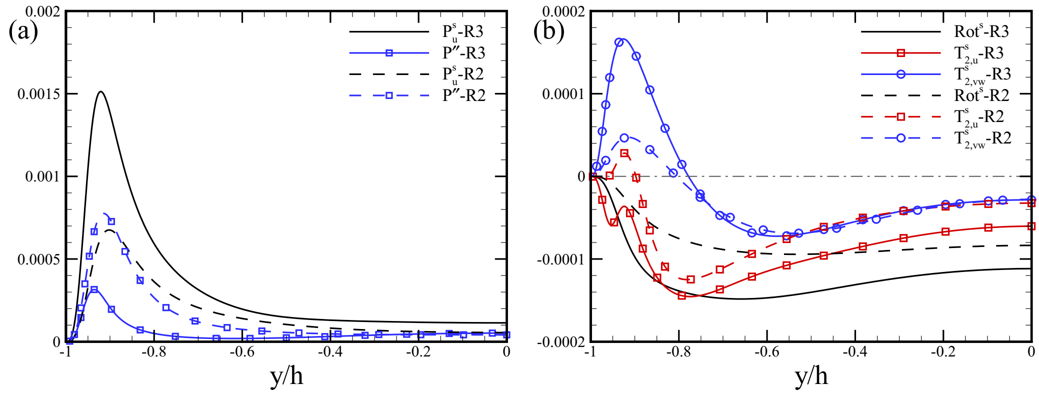

FIG. 13. (a) Production terms of the secondary flows P^s_u and the residual flows P'' from two different states; (b) energy transfer terms Rot^s, $T^s_{2,u}$, and $T^s_{2,vw}$ from two different states. All quantities are normalized by $8U_w^3/h$.

secondary flows, the cross-flow part of the secondary flows, and the residual field. It is seen from Fig. 13(a) that the secondary flows draw much more energy, through the production term, from the mean field at the $R3$ state than that at the $R2$ state, while the residual field draws more energy from the mean field at the $R2$ state. Furthermore, the peak of the production terms for the residual field is located closer to the wall at both states, illustrating that the activities of the residual field occur closer to the wall. The larger P^s_u will be accompanied by larger k^s_u, ϵ^s_u, $T^s_{2,u}$, and Rot^s at the $R3$ state, as depicted in Figs. 12(a) and 13(b), where the profiles of the energy transfer terms among the three shares at both states are shown. For the energy transfer term between the streamwise part and the cross-flow part of the secondary field, Rot^s, it is negative across the channel, and the energy is transferred from the streamwise part to the cross-flow part in the whole channel. The absolute value at the $R3$ state is larger than that at the $R2$ state, which is consistent with the Reynolds shear profile $\langle u^s v^s \rangle$ shown in Fig. 12(b) since $\mathrm{Rot}^s = \mathrm{Ro}\langle u^s v^s \rangle$. For the energy exchange term between the streamwise part of the secondary flows and the residual field, $T^s_{2,u}$, the general patterns are the same at two states, that is, there are two maxima in absolute values in the profile, one located around $y \approx -0.95h$ and the other around $y \approx -0.8h$. However, the difference between the two states is also obvious. At the $R3$ state, $T^s_{2,u}$ is negative across the channel, documenting that the term acts as a sink of energy in the balance equation of k^s_u and the energy is transferred from the streamwise secondary flows to the residual field across the channel. However, $T^s_{2,u}$ is positive within the range $-0.95 < y/h < -0.85$ at the $R2$ state. This means an inverse energy cascade, i.e., the energy is taken from the residual field and fed into the streamwise secondary flow in this region as reported by Bech and Andersson [5]. For the energy exchange between the cross-flow part of the secondary flows and the residual field, $T^s_{2,vw}$, its behavior is different from $T^s_{2,u}$, and it is positive in the near wall region $y/h \lesssim -0.8$ while it is negative farther away from the wall at both states, illustrating that this term acts as a source in the near wall region while it behaves as a sink outward and the

TABLE III. Wall-normal averaged quantities from the balance equations of k^s_u, k^s_{vw}, and k'' from two different states. All quantities are normalized by $8U_w^3/h$ and amplified by 10^4.

	k^s_u				k^s_{vw}		k''		
States	$[P^s_u]_y$	$-[\epsilon^s_u]_y$	$[T^s_{2,u}]_y$	$[\mathrm{Rot}^s]_y$	$-[\epsilon^s_{vw}]_y$	$[T^s_{2,vw}]_y$	$[P'']_y$	$-[\epsilon'']_y$	$[T''_2]_y$
$R3$	3.255	−1.152	−0.898	−1.206	−1.023	−0.181	0.577	−1.658	1.079
$R2$	1.756	−0.398	−0.578	−0.781	−0.447	−0.331	1.446	−2.358	0.909

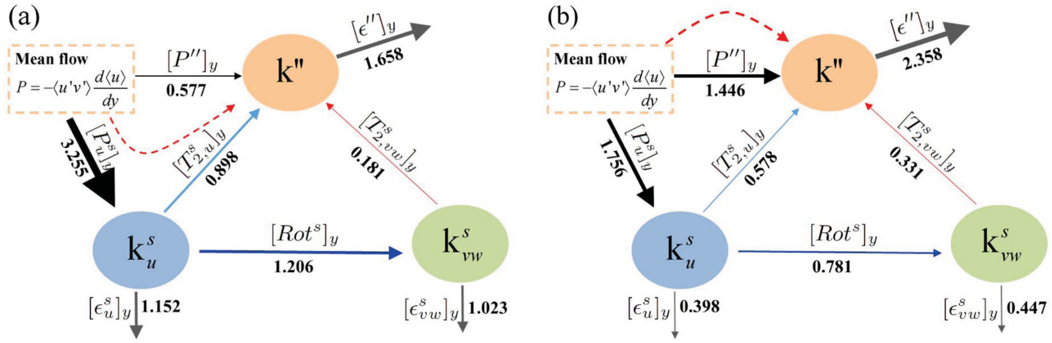

FIG. 14. Time-volume-averaged balance equations for the kinetic energy k^s_u, k^s_{vw}, and k'' at two different states: (a) $R3$ state and (b) $R2$ state. The arrows show the directions of the kinetic energy transfer and their relative magnitudes. The corresponding absolute magnitudes of the transfer terms are shown by the numbers. The dashed line at two panels shows the main routine of the energy transferred from the mean field to the residual field: the kinetic energy that is transferred from the mean field to the residual field is mainly transferred through the streamwise component of the secondary flow at the $R3$ state, while it is mainly transferred through the production term at the $R2$ state. All quantities are normalized by $8U_w^3/h$ and amplified by 10^4.

cross-part of the secondary flow can draw energy from the residual field in the near wall region. Although in the region $-0.8 \lesssim y/h \lesssim 0$, $T^s_{2,vw}$ is almost the same at both states, it is much stronger at the $R3$ state in the near wall region, and thus the overall energy transfer from the cross-flow of the secondary field to the residual field at the $R3$ state is less.

To see the energy transfer more clearly, the wall-normal averaged quantities of the time-volume-averaged balance equations of all three shares are calculated and listed in Table III. A sketch of the energy transfer between three shares is also displayed in Fig. 14. The general information is the same as the profiles shown in Fig. 13. It is evident that $[T^s_{2,u}]_y$ is larger than $[T^s_{2,vw}]_y$ at both states, and this is due to the apparent inverse energy cascade observed in the near wall region at both states for $T^s_{2,vw}$. An important point to notice is that the energy incomes for the residual field at two states are different. At the $R3$ state, the energy is mainly transferred from the secondary flow field through $[T^s_{2,u}]_y$, and only around 1/3 is it directly received from the mean field. On the contrary, more than 60% of the energy is directly drawn from the mean field at the $R2$ state through $[P'']_y$ and the mean field is the main direct energy source for the residual field. This result again supports the concept that the large-scale secondary flows play a very critical role in these two states, as conjectured in Ref. [40].

V. SUMMARY

In this paper, the dual-state phenomenon of RPCF is studied. Differently from our previous work [14], where the multiple states in RPCF and the corresponding basic flow statistics were reported, we investigated the influence of the initial flow field and turbulent statistics related to balances of Reynolds stresses in the present work, aiming to explore the role of the large-scale structures at the two different states.

To study the influence of the initial flow field, nine new initial flow fields are constructed by the superposition of the two instantaneous flow fields at two different states. Our simulation results show that the flow can finally evolve to both states depending on the weight parameter α used in the initial field construction. A boundary exists in the range $0.6 < \alpha < 0.7$ according to the results, and this further documents that the dual states of RPCF with the present parameters, i.e., $\mathrm{Re}_w = 1300$ and $\mathrm{Ro} = 0.2$, are very robust. Furthermore, the mean velocity and Reynolds stresses from these nine simulations coincide with the previous results at the same state.

In the study of the Reynolds stress balances, it is found that there are no dominant balances of the terms for all four nonzero components at both states. Generally, the profiles of the terms at both states have the same shape while the amplitudes are different. The state with more roll cells (three pairs of roll cells with $L_z = 4\pi h$, $R3$) has a larger amplitude, and thus a larger wall-normal averaged value in the production term. This is consistent with larger turbulent kinetic energy and dissipation at this state.

To further study the differences, the flow is decomposed into four parts through a quad-decomposition, including the mean part, the streamwise part, and the cross-flow parts of the secondary flow field and the residual field, which is the fluctuation field subtracting the secondary flow field. It is found that at the more energetic $R3$ state, the secondary flow is much stronger than that at the $R2$ state while the corresponding residual field is weaker. At the $R3$ state, the kinetic energy drawn from the mean field is mainly transferred to the secondary flow field, and only a small share is transferred directly to the residual field. At this state, the energy income for the residual field is mainly from the secondary flow field through the energy transfer term $T^s_{2,u}$ and $T^s_{2,vw}$. On the contrary, the energy transferred from the mean field to the secondary flow field and to the residual field is comparable at the $R2$ state, and the energy from the mean field becomes the main source for the residual field. Also, a local inverse energy cascade is observed in the near wall region at the $R2$ state where the energy is transferred from the residual field back to the streamwise part of the secondary field. These results support the concept that the large-scale secondary flows play a very critical role in these two states.

Finally, we would like to emphasize that the present study is based on a single computational domain size with the same grid resolution. The Reynolds number and rotation number were also kept fixed, although Huang *et al.* [46] had shown that multiple states could exist at a very wide rotation number range at the same Reynolds number. In the future, the influences of computational domain size and Reynolds number will be investigated.

ACKNOWLEDGMENTS

This work was supported by the National Science Foundation of China (NSFC Grants No. 11822208, No. 11772297, No. 91752201, and No. 91752202). Z.H. Xia would also like to thank the support from the Fundamental Research Funds for the central Universities. The simulations were run on the TH-2A supercomputer in Guangzhou.

[1] J. P. Johnston, R. M. Halleen, and D. K. Lezius, Effects of spanwise rotation on the structure of two-dimensional fully developed turbulent channel flow, J. Fluid Mech. **56**, 533 (1972).

[2] R. Kristoffersen and H. I. Andersson, Direct simulations of low-Reynolds-number turbulent flow in a rotating channel, J. Fluid Mech. **256**, 163 (1993).

[3] O. Grundestam, S. Wallin, and A. V. Johansson, Direct numerical simulations of rotating turbulent channel flow, J. Fluid Mech. **598**, 177 (2008).

[4] Z. Xia, Y. Shi, and S. Chen, Direct numerical simulation of turbulent channel flow with spanwise rotation, J. Fluid Mech. **788**, 42 (2016).

[5] K. H. Bech and H. I. Andersson, Secondary flow in weakly rotating turbulent plane Couette flow, J. Fluid Mech. **317**, 195 (1996).

[6] K. H. Bech and H. I. Andersson, Turbulent plane Couette flow subject to strong system rotation, J. Fluid Mech. **347**, 289 (1997).

[7] T. Tsukahara, N. Tillmark, and P. H. Alfredsson, Flow regimes in a plane Couette flow with system rotation, J. Fluid Mech. **648**, 5 (2010).

[8] T. Kawata and P. H. Alfredsson, Experiments in rotating plane Couette flow—Momentum transport by coherent roll-cell structure and zero-absolute-vorticity state, J. Fluid Mech. **791**, 191 (2016).

[9] J. Gai, Z. H. Xia, Q. D. Cai, and S. Y. Chen, Turbulent statistics and flow structures in spanwise-rotating turbulent plane Couette flows, Phys. Rev. Fluids **1**, 054401 (2016).

[10] M. Barri and H. I. Andersson, Anomalous turbulence in rapidly rotating plane Couette flow, in *Advances in Turbulence XI*, edited by J. M. L. M. Palma and A. S. Lopes (Springer-Verlag, Berlin, 2007), pp. 100–102.

[11] M. Barri and H. I. Andersson, Computer experiments on rapidly rotating plane Couette flow, Commun. Comput. Phys. **7**, 683 (2010).

[12] T. Tsukahara, Structures and turbulent statistics in a rotating plane Couette flow, J. Phys.: Conf. Ser. **318**, 022024 (2011).

[13] M. Salewski and B. Eckhardt, Turbulent states in plane Couette flow with rotation, Phys. Fluids **27**, 045109 (2015).

[14] Z. Xia, Y. Shi, Q. Cai, M. Wan, and S. Chen, Multiple states in turbulent plane Couette flow with spanwise rotation, J. Fluid Mech. **837**, 477 (2018).

[15] N. Tillmark and P. H. Alfredsson, Experiments on rotating plane Couette flow, in *Advances in Turbulence VI*, edited by S. Gavrilakis, L. Machiels, and P. A. Monkewitz (Kluwer, Dordrecht, The Netherlands, 1996), pp. 391–394.

[16] P. H. Alfredsson and N. Tillmark, Instability, transition and turbulence in plane Couette flow with system rotation, in *Laminar Turbulent Transition and Finite Amplitude Solutions*, edited by T. Mullin and R. R. Kerswell (Springer-Verlag, Berlin, 2005), pp. 173–193.

[17] K. Hiwatashi, P. H. Alfredsson, N. Tillmark, and M. Nagata, Experimental observations of instabilities in rotating plane Couette flow, Phys. Fluids **19**, 048103 (2007).

[18] A. Suryadi, A. Segalini, and P. H. Alfredsson, Zero absolute vorticity: Insight from experiments in rotating laminar plane Couette flow, Phys. Rev. E **89**, 033003 (2014).

[19] T. Kawata and P. H. Alfredsson, Turbulent rotating plane Couette flow: Reynolds and rotation number dependency of flow structure and momentum transport, Phys. Rev. Fluids **1**, 034402 (2016).

[20] Y. H. Huang, Z. Xia, M. P. Wan, Y. Shi, and S. Chen, Numerical investigation of plane Couette flow with weak spanwise rotation, Sci. China Phys. Mech. Astron. **62**, 044711 (2019).

[21] T. B. Benjamin and T. Mullin, Notes on the multiplicity of flows in the Taylor experiment, J. Fluid Mech. **121**, 219 (1982).

[22] Y. Kachanov, Physical mechanisms of laminar-boundary-layer transition, Annu. Rev. Fluid Mech. **26**, 411 (1994).

[23] C. Lee and J. Wu, Transition in wall-bounded flows, Appl. Mech. Rev. **61**, 030802 (2008).

[24] C. Andereck, S. Liu, and H. Swinney, Flow regimes in a circular Couette system with independently rotating cylinders, J. Fluid Mech. **164**, 155 (1986).

[25] B. Martínez-Arias, J. Peixinho, O. Crumeyrolle, and I. Mutabazi, Effect of the number of vortices on the torque scaling in Taylor-Couette flow, J. Fluid Mech. **748**, 756 (2014).

[26] B. Eckhardt, T. M. Schneider, B. Hof, and J. Westerweel, Turbulence transition in pipe flow, Annu. Rev. Fluid Mech. **39**, 447 (2007).

[27] F. Ravelet, L. Marié, A. Chiffaudel, and F. Daviaud, Multistability and Memory Effect in a Highly Turbulent Flow: Experimental Evidence for a Global Bifurcation, Phys. Rev. Lett. **93**, 164501 (2004).

[28] F. Revelet, A. Chiffaudel, and F. Daviaud, Supercritical transition to turbulence in an inertially driven von Kármán closed flow, J. Fluid Mech. **601**, 339 (2008).

[29] P. P. Cortet, A. Chiffaudel, F. Daviaud, and B. Dubrulle, Experimental Evidence of a Phase Transition in a Closed Turbulent Flow, Phys. Rev. Lett. **105**, 214501 (2010).

[30] H. Xi and K. Xia, Flow mode transitions in turbulent thermal convection, Phys. Fluids **20**, 055104 (2008).

[31] E. P. van del Poel, R. J. A. M. Stevens, and D. Lohse, Connecting flow structures and heat flux in turbulent Rayleigh-Bénard convection, Phys. Rev. E **84**, 045303(R) (2011).

[32] G. Ahlers, D. Funfschilling, and E. Bodenschatz, Heat transport in turbulent Rayleigh-Bénard convection for $\mathrm{Pr} \simeq 0.8$ and $\mathrm{Ra} \lesssim 10^{15}$, J. Phys.: Conf. Ser. **318**, 082001 (2011).

[33] S. Grossmann and D. Lohse, Multiple scaling in the ultimate regime of thermal convection, Phys. Fluids **23**, 045108 (2011).

[34] S. Weiss and G. Ahlers, Effect of tilting on turbulent convection: cylindrical samples with aspect ratio $\Gamma = 0.50$, J. Fluid Mech. **715**, 314 (2013).
[35] Y. C. Xie, G. Y. Ding, and K. Q. Xia, Flow Topology Transition via Global Bifurcation in Thermally Driven Turbulence, Phys. Rev. Lett. **120**, 214501 (2018).
[36] D. Zimmerman, S. A. Triana, and D. Lathrop, Bi-stability in turbulent, rotating spherical Couette flow, Phys. Fluids **23**, 065104 (2011).
[37] K. P. Iyer, F. Bonaccorso, L. Biferale, and F. Toschi, Multiscale anisotropic fluctuations in sheared turbulence with multiple states, Phys. Rev. Fluids **2**, 052602(R) (2017).
[38] N. Yokoyama and M. Takaoka, Hysteretic transitions between quasi-two-dimensional flow and three-dimensional flow in forced rotating turbulence, Phys. Rev. Fluids **2**, 092602(R) (2017).
[39] Y. Yang, R. Verzicco, and D. Lohse, Multiple equilibria in fingering double diffusive convection turbulence, arXiv:1904.09519.
[40] S. Huisman, R. van der Veen, C. Sun, and D. Lohse, Multiple states in highly turbulent Taylor-Couette flow, Nat. Commun. **5**, 3820 (2014).
[41] S. Grossmann, D. Lohse, and C. Sun, High-Reynolds number Taylor-Couette turbulence, Annu. Rev. Fluid Mech. **48**, 53 (2016).
[42] R. Ostilla-Mónico, D. Lohse, and R. Verzicco, Effect of roll number on the statistics of turbulent Taylor-Couette flow, Phys. Rev. Fluid **1**, 054402 (2016).
[43] R. C. A. van der Veen, S. G. Huisman, O.-Y. Dung, H. L. Tang, C. Sun, and D. Lohse, Exploring the phase space of multiple states in highly turbulent Taylor-Couette flows, Phys. Rev. Fluids **1**, 024401 (2016).
[44] M. Gul, G. Elsinga, and J. Westerweel, Experimental investigation of torque hysteresis behavior of Taylor-Couette flow, J. Fluid Mech. **836**, 635 (2018).
[45] D. Wilcox, *Turbulence Modeling for CFD*, 3rd ed. (DCW Industries, 2006), p. 5.
[46] Y. Huang, Z. Xia, M. Wan, Y. Shi, and S. Chen, Hysteresis behavior in spanwise rotating plane Couette flow with varying rotation rates, Phys. Rev. Fluids **4**, 052401(R) (2019).
[47] B. Launder, D. P. Tselepidakis, and B. Younis, A second-moment closure study of rotating channel flow, J. Fluid Mech. **183**, 63 (1987).
[48] J. Gai, Direct numerical simulations of spanwise-rotating turbulent plane Couette flow, Ph.D. thesis, College of Engineering, Peking University, Beijing (2016).
[49] R. D. Moser and P. Moin, The effects of curvature in wall-bounded turbulent flows, J. Fluid Mech. **175**, 479 (1987).
[50] M. J. Lee and J. Kim, The structure of turbulence in a simulated plane Couette flow, in *Proceedings of Eighth Symposium on Turbulent Shear Flows*, edited by F. Durst *et al.* (Munich, Germany, 1991), paper 5-3.
[51] Q. D. Cai, J. Gai, Z. Sun, and Z. H. Xia, Quad-decomposition of velocity field in spanwise-rotating turbulent plane Couette flows, Int. J. Nonlin. Sci. Numer. Simul. **17**, 305 (2016).